Supporting Information

Immobilisation of a molecular iridium complex on periodic mesoporous organosilica for heterogeneous water oxidation catalysis

Raúl Rojas-Luna,*[a,b] Juan Amaro-Gahete,[b,c] Sumit Konar,[a] Francisco J Romero-Salguero,[b] Dolores Esquivel,*[b] Souvik Roy,*[a]

[a]*Department of Chemistry, School of Natural Sciences, University of Lincoln, Green Lane, Lincoln, Lincolnshire, LN6 7DL, UK.*

[b]*Departamento de Química Orgánica, Instituto Químico para la Energía y el Medioambiente (IQUEMA), Facultad de Ciencias, Universidad de Córdoba, Campus de Rabanales, Edificio Marie Curie, E-14071 Córdoba, Spain.*

[c]*UGR-Carbon – Materiales Polifuncionales Basados en Carbono, Departamento de Química Inorgánica, Unidad de Excelencia Química Aplicada a Biomedicina y Medioambiente, Universidad de Granada, ES18071 Granada, Spain*

Email: rrojas-luna@lincoln.ac.uk (Raúl Rojas-Luna), q12esmem@uco.es (Dolores Esquivel), sroy@lincoln.ac.uk (Souvik Roy)

Table of Contents

1. Experimental Section

Chemical reagents. Chemical reagents and solvents in this work were used without further purification, including (pentamethylcyclopentadienyl)iridium(III) chloride dimer (97%, TCI), ammonium cerium(IV) nitrate (CAN, 97%, TCI), dry ethanol (Supelco), methylsulfonylmethane (MSM, 99%, Fluorochem), nitric acid (69%, Panreac), N,N-dimethylformamide (Pure, Panreac), ethanol absolute (EtOH, Fischer, ≥99.8%), acetonitrile (MeCN, Fischer, ≥99.8%), dichloromethane (DCM, 99.9%, Labkem). Deuterated solvents for NMR (D_2O and CD_3CN) were purchase from Eurisotop.

Characterisation techniques. X-ray diffraction patterns (XRD) were measured on a Bruker D8 Discover A25 diffractometer using Cu-Kα radiation (λ = 1.5418 Å) in the 2θ range of 0.5–5°. Nitrogen adsorption/desorption isotherms were obtained at liquid nitrogen temperature (−196 °C) using a Micromeritics ASAP 2420 instrument. Samples were degassed at 120 °C overnight before measurements. Specific surface area (S_{BET}) was calculated from the adsorption data using Brunauer-Emmett-Teller (BET) method, and the pore size distribution was estimated using the density functional theory (DFT) equilibrium model. Conventional TEM and STEM were performed using a FEI Talos F200i S/TEM microscope operating at 200 kV. Elemental mappings were recorded using energy dispersive X-ray spectroscopy (EDS). UV–vis spectra were acquired on a Shimadzu UV-1800 Spectrophotometer using quartz glass cuvettes (1 cm path length). UV–vis diffuse reflectance spectra were collected using a Perkin Elmer Lambda 650 S UV–vis spectrometer with a 150 mm integrating sphere. In situ UV–vis spectroscopy was performed on a AvaSpec-ULS2048 fiber optics spectrometer using a AvaLight-DHc light source equipped with deuterium and halogen lamps. DLS data were acquired on a Malvern Zetasizer Nano ZSP particle analyser with a 632.8 nm red laser (He–Ne). Raman spectra were acquired using a Bruker Senterra Raman microscope using 785 nm laser excitation and a 50× objective lens. The spectrometer was calibrated using a polystyrene standard. Fourier transform infrared spectroscopy (FTIR) was

performed on a Perkin-Elmer 2000 FTIR spectrometer. Measurements were conducted on pellets by mixing the sample (1 wt%) with KBr. Nuclear magnetic resonance (NMR) spectra were collected using a Bruker AVANCE III HD at 500 MHz. NMR data was taken in the ppm unit and referenced against the solvent residual peaks. Coupling constants (J) are reported in Hertz (Hz). Coupling patterns are indicated as s (singlet), d (doublet), t (triplet), dd (doublet of doublet), ddd (doublet of doublet of doublet), td (triplet of doublet), dt (doublet of triplet). Solid-state ^{13}C cross polarization magic-angle spinning (CP/MAS) NMR were acquired on a Bruker Avance III HD 400 WB spectrometer. Tetramethylsilane (TMS) standard was used as chemical shift reference X-ray photoelectron spectroscopy (XPS) was performed using a PHI VersaProbe II spectrometer using a monochromatic Al Kα X-ray source (1486.6 eV). C 1s electron at 284.8 eV was used as a standard reference to calibrate the photoelectron energy shift. Iridium content of the catalyst was analysed by inductively coupled plasma mass spectrometry (ICP-MS, Perkin-Elmer NexION 350X). CHN elemental analysis were determined in an elemental microanalyzer Thermo Finnigan Flash EA 1112 series with a Micro TruSpec detection system from LECO. HRMS was performed in electrospray positive ion mode using a Thermo Exactive Plus Orbitrap Mass Spectrometer.

Single-Crystal X-ray diffraction. Single crystals suitable for X-ray diffraction measurements were mounted on MiTeGen Dual-Thickness MicroMounts and analysed using a Bruker D8 Venture diffractometer with a photon detection system. Unit cell measurements and data collections were performed at 173 K using Cu Kα radiation (λ = 1.54056 Å). Crystal data and refinement parameters are presented in Table S1 in the Supporting Information. Using Olex2,[1] the structure was solved with the SHELXT[2] structure solution program using Intrinsic Phasing and refined with the SHELXL[3] refinement package using Least Squares minimisation.

Electrochemical measurements. A conventional three-electrode cell setup along with a Biologic VSP-300 potentiostat was employed for the electrochemical measurements. Cyclic voltammetry (CV) and Differential Pulse Voltammetry

(DPV) data for [IrCp*Cl(dppz)]Cl complex (1 mM) were collected in homogeneous phase under nitrogen by using a glassy carbon working electrode (GCE, 3 mm diameter), a Pt-wire counter electrode and specific reference electrodes based on solution phase. Before measurements, the GCE was mirror-polished with an alumina slurry (0.3 micron particle size) and washed with deionized water. For aqueous conditions, an Ag/AgCl reference electrode with saturated KCl (3M) was employed, with either HNO_3 (0.1M, pH = 1) or buffered phosphate (0.1M) solutions, adjusted to the desired pH, as the electrolyte. Potentials were referenced to the normal hydrogen electrode (NHE) by using the conversion $E_{NHE} = E_{Ag/AgCl} + 0.197$ V. In organic media, a non-aqueous $Ag|Ag^+$ (10 mM $AgNO_3$ in MeCN) reference electrode was employed in 0.1 M tetrabutylammonium tetrafluoroborate ($TBABF_4$) supporting electrolyte. Voltammograms in the organic phase are reported against ferrocenium/ferrocene ($Fc^{+/0}$) couple using ferrocene as an internal standard.

2. Supporting Figures

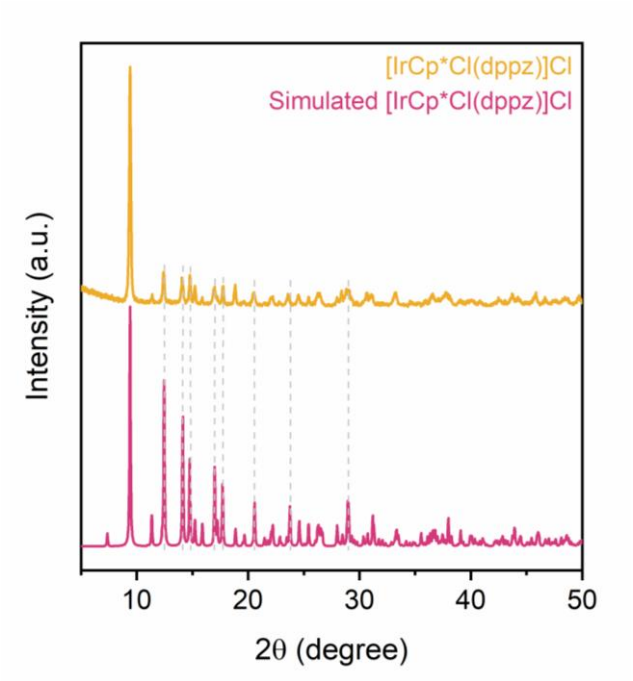

Figure S1. XRD patterns of [IrCp*Cl(dppz)]Cl and simulated [IrCp*Cl(dppz)]Cl data from crystal structure.

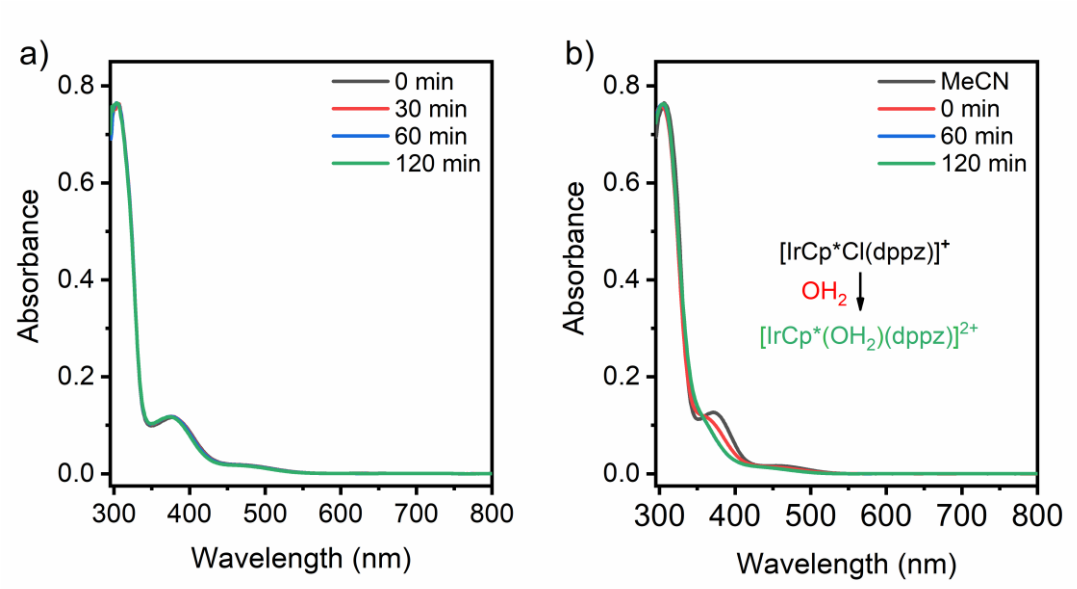

Figure S2. UV–vis spectra of [IrCp*Cl(dppz)]Cl (2.5×10^{-5} M) in (a) non-aqueous MeCN solution and (b) aqueous HNO_3 (0.1M, pH = 1.0) solution.

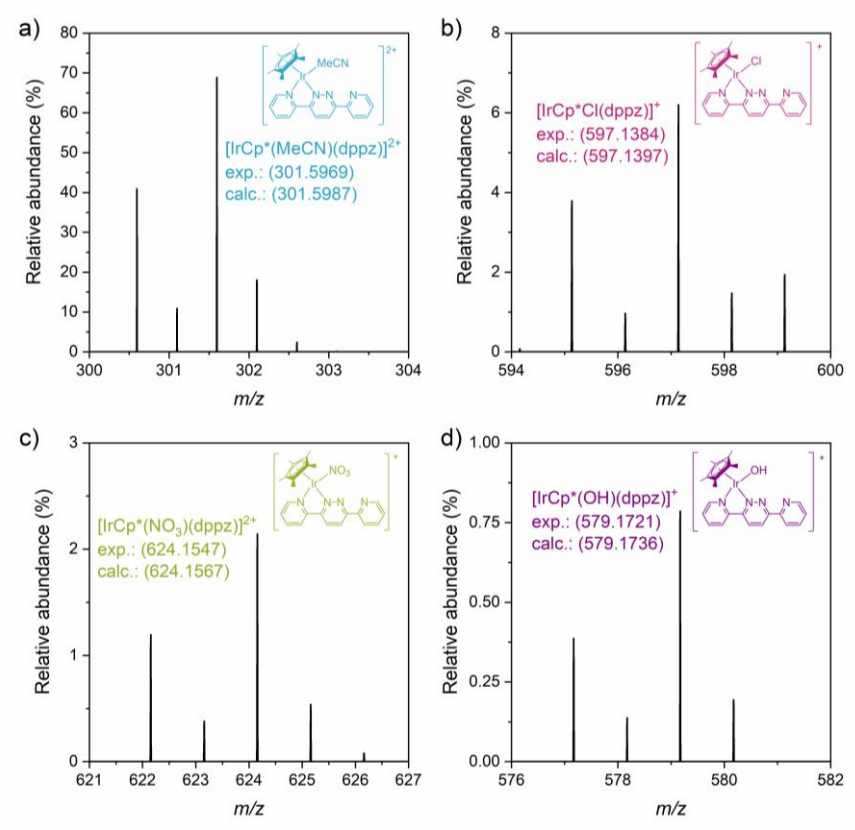

Figure S3. Mass spectrum of [IrCp*Cl(dppz)Cl]Cl in solution showing molecular ion peaks for (a) $[IrCp^*(MeCN)(dppz)]^{2+}$, (b) $[IrCp^*Cl(dppz)]^{+}$, (c) $([IrCp^*(NO_3)(dppz)]^{2+}$, and (d) $[IrCp^*(OH)(dppz)]^{+}$. HRMS was performed in a mixed water/MeCN solvent (1:1). $[IrCp^*(OH)(dppz)]^{+}$ species was detected exclusively under fully aqueous conditions.

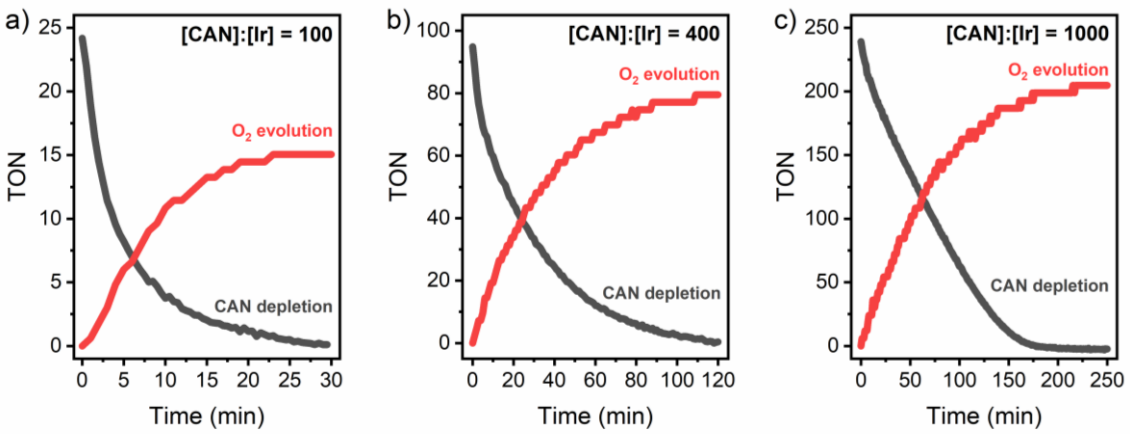

Figure S4. Kinetic profile of CAN depletion (black trace) and O_2 evolution (red trace) for [IrCp*Cl(dppz)]Cl (10 μM). The turnover number (TON) for Ce^{IV} depletion is defined as the ratio of the number of oxidizing equivalents consumed, divided by four, to the moles of catalyst, since one catalytic cycle requires the consumption of 4 moles of Ce^{IV}.

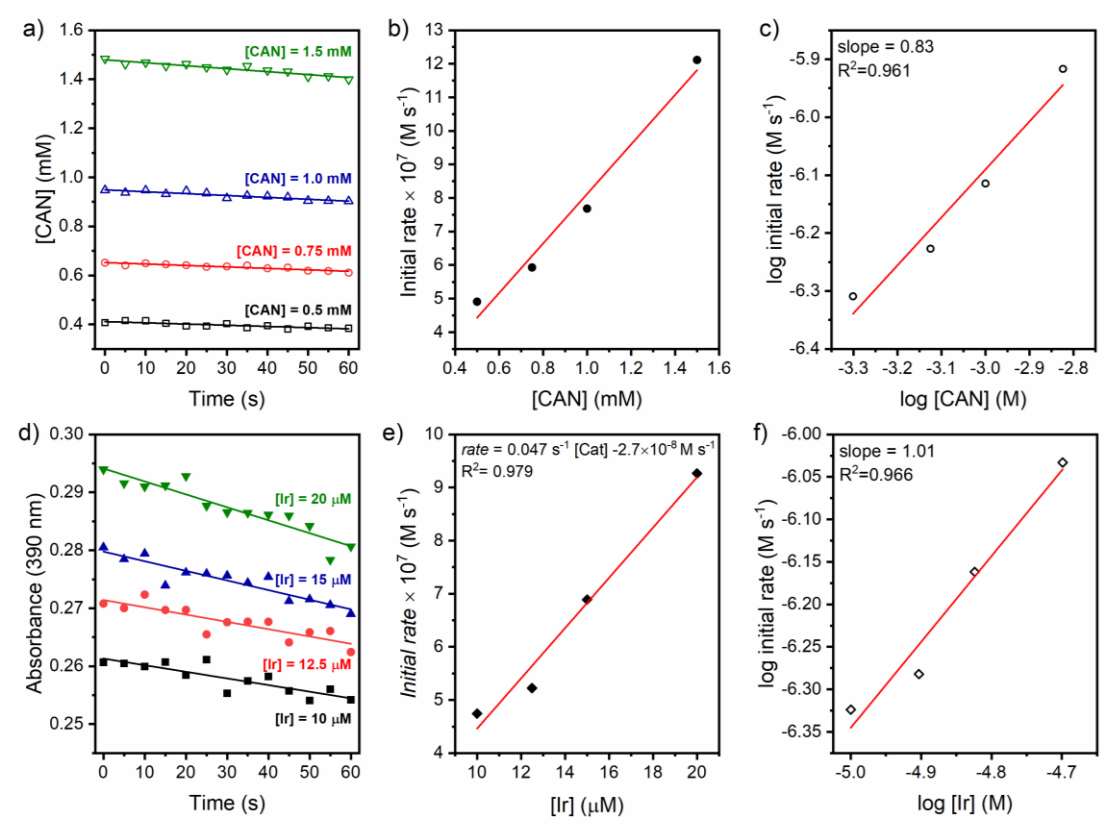

Figure S5. (a) CAN concentration decay over time at fixed 10μM of [IrCp*Cl(dppz)]Cl and different concentrations of CAN (0.5–1.5 mM) in 0.1 M HNO_3. CAN concentration was determined by monitoring CAN absorbance decay at 390 nm and its subsequent conversion through Lambert–Beer law. (b) Plot of the initial rates versus oxidising agent concentration. (c) Decimal logarithm of initial rate of CAN depletion versus decimal logarithm of CAN concentration. (d) CAN absorbance decay over time at fixed 1 mM concentration of CAN and different [IrCp*Cl(dppz)]Cl concentrations (10–20 μM) in 0.1 M HNO_3. (e) Plot of the initial rates versus catalyst concentration. (f) Decimal logarithm of initial rate of CAN depletion versus decimal logarithm of catalyst concentration.

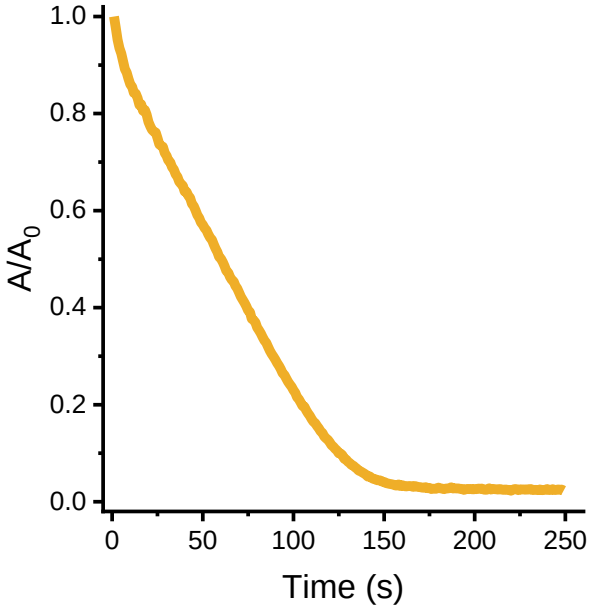

Figure S6. CAN depletion monitoring at 390 nm for a 10 mM solution of CAN (0.1 M HNO_3, pH = 1) containing [IrCp*Cl(dppz)]Cl] (10 μM).

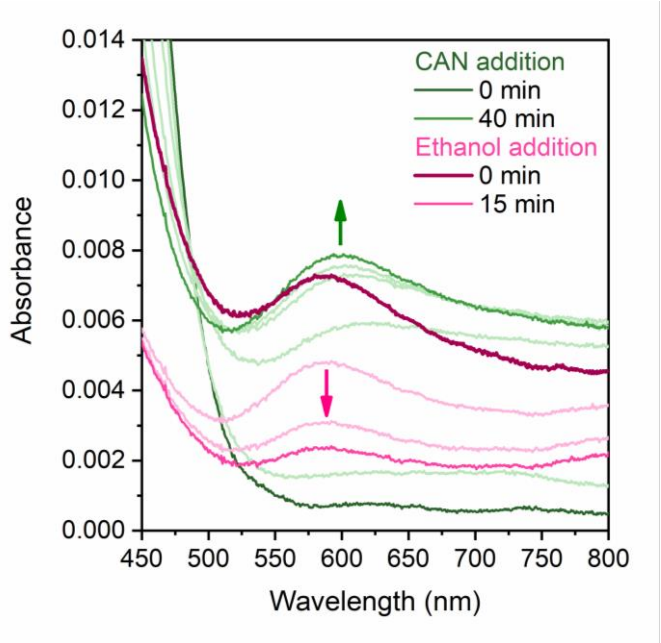

Figure S7. UV–vis spectra evolution over time in the range of 450–800 nm of a solution containing [IrCp*Cl(dppz)]Cl (10 μM) and CAN (1 mM, 100 equiv) in 0.1 M HNO_3 aqueous solution (green traces). Addition of ethanol (50 μL) showed absorbance decay of the generated Ir species (pink traces).

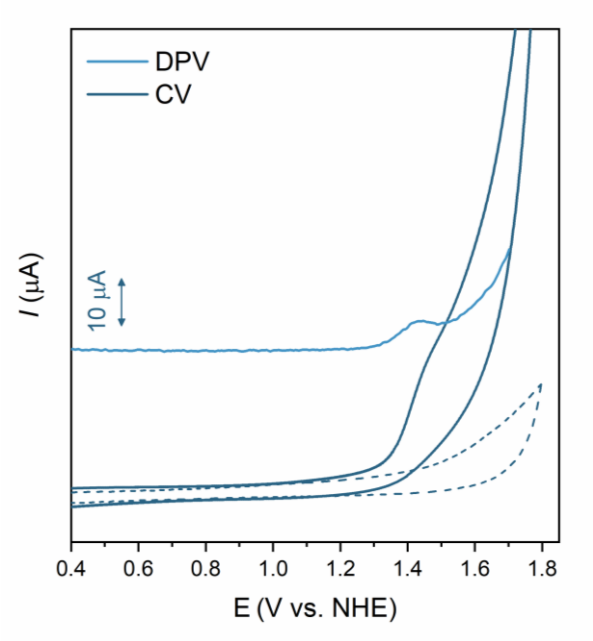

Figure S8. Cyclic voltammogram and differential pulse voltammetry (pulse height = 50 mV, pulses width = 50 ms, step height = 5 mV, step time = 10 s) for [IrCp*Cl(dppz)]Cl at pH 7. Conditions: glassy carbon working electrode, Ag/AgCl/KCl (3M) reference electrode, Pt wire counter electrode, 0.1 M electrolyte, and a scan rate of 100 mV s^{-1}. Dashed traces indicate background measurements.

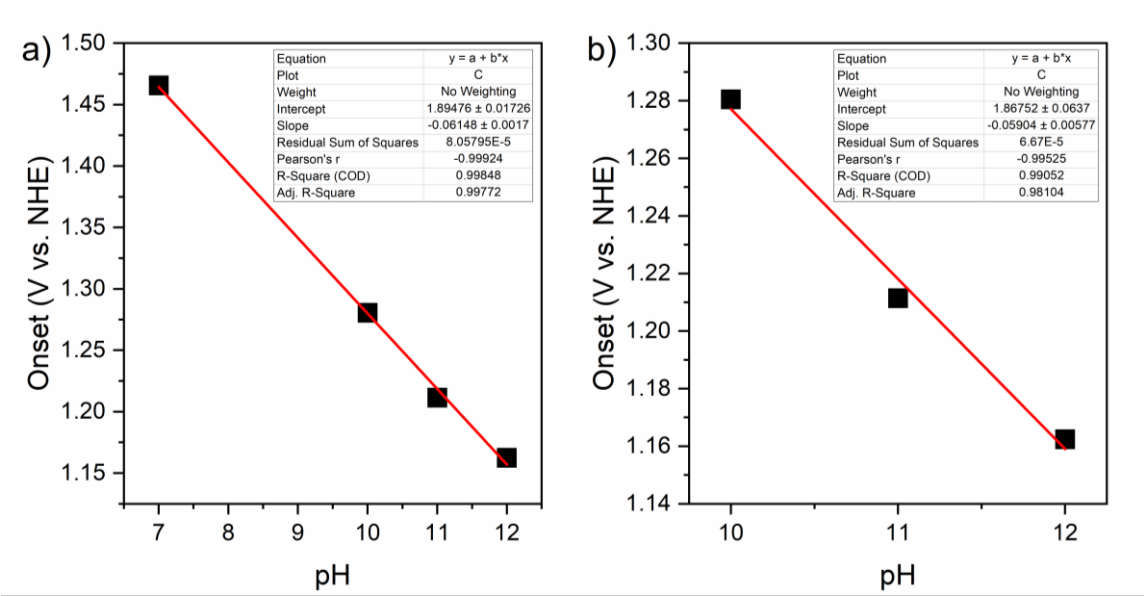

Figure S9. Linear fits for onset potentials for [IrCp*Cl(dppz)]Cl versus pH in two ranges: (a) 7–12 and (b) 10–12. The data for pH 7 is omitted in Figure S9b because of the interference from another oxidation step at ~1.4 V vs NHE, as shown in Figure S8. The onset potential was determined at 40 µA current. The voltammetry data used for deriving this plot are shown in Figure 2a in the main manuscript.

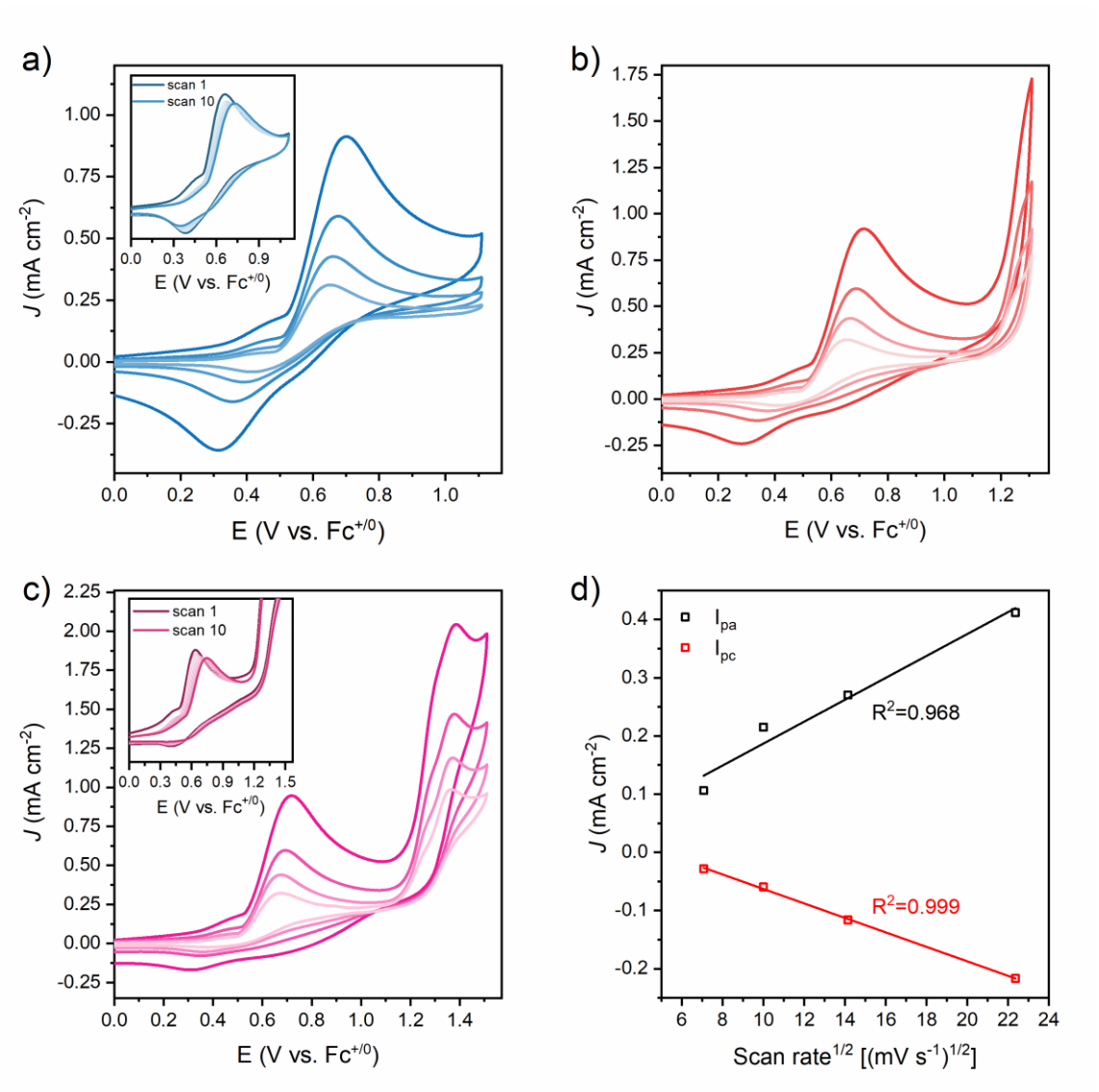

Figure S10. (a-c) Scan rate dependent (500, 200, 100 and 50 mV s^{-1}) cyclic voltammograms of [IrCp*Cl(dppz)]Cl in acetonitrile at different potential windows. The insets show consecutives CVs (10 scans) of [IrCp*Cl(dppz)]Cl at 100 mV s^{-1}. (d) Correlation of the linear fit between the peak current density of the redox process showed in (a) with the scan rate. Conditions: glassy carbon working electrode, Pt wire counter electrode, Ag/$AgNO_3$ (10 mM) reference electrode, and $TBABF_4$ (0.1 M) supporting electrolyte.

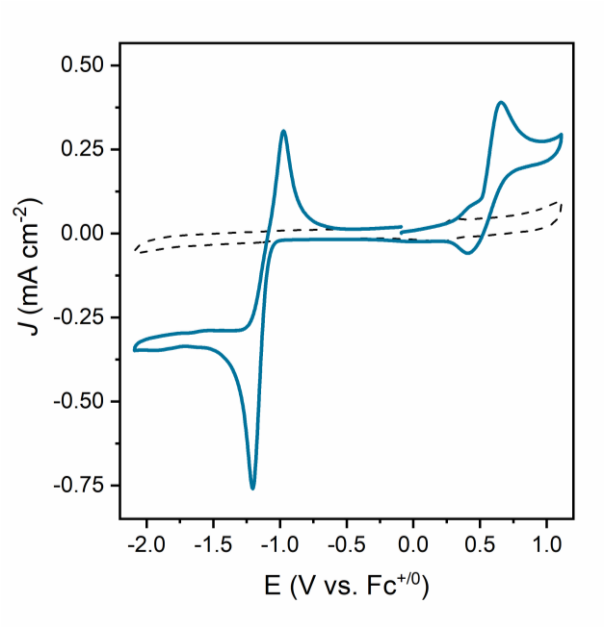

Figure S11. Cyclic voltammograms of [IrCp*Cl(dppz)]Cl (1.0 mM) in MeCN. Dashed trace indicates background measurement.

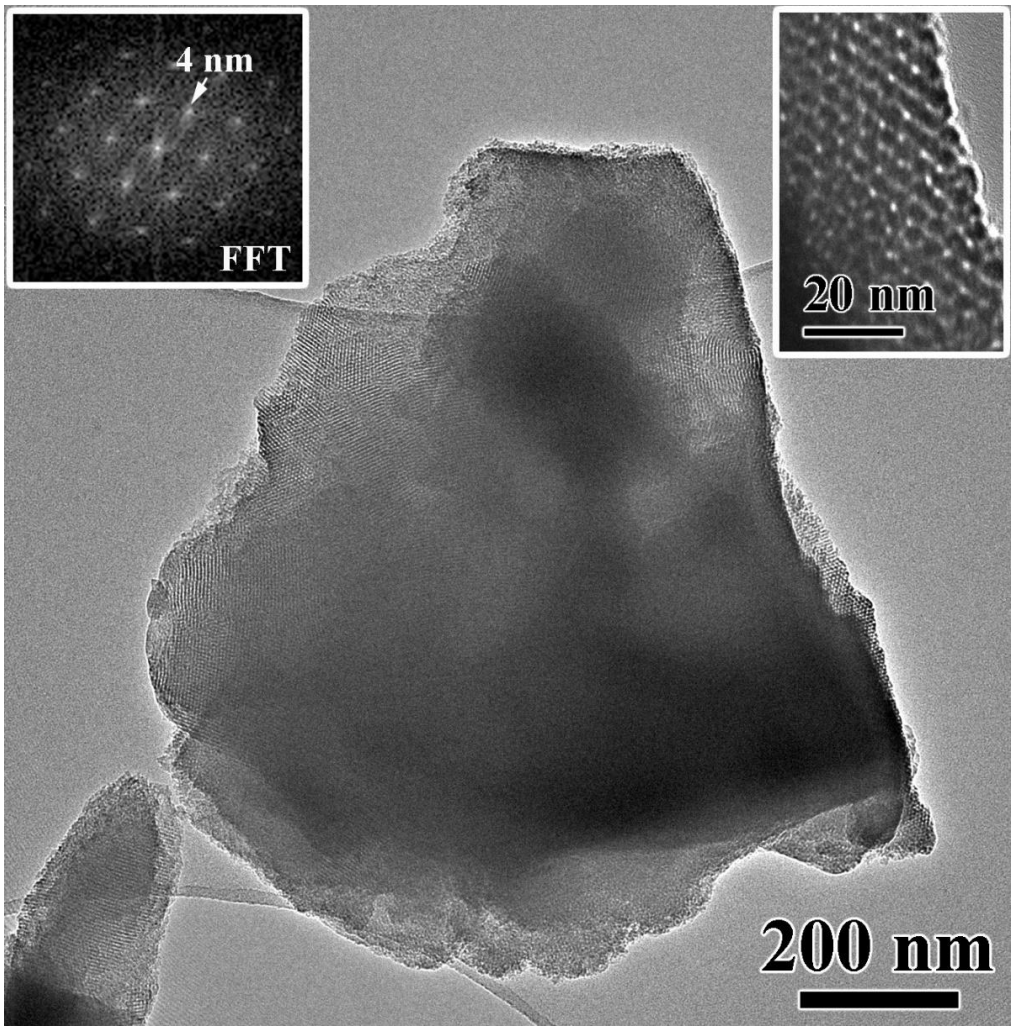

Figure S12. TEM image of Ir-PMO. Highly ordered hexagonal arrangement are displayed in the magnification (upper right inset) and its corresponding FFT diagram (upper left inset).

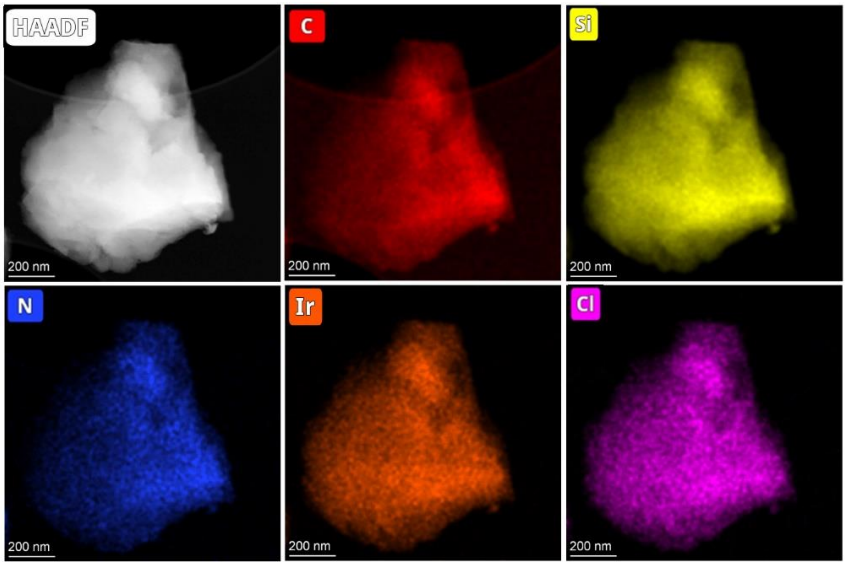

Figure S13. HAADF-STEM image and EDS elemental mapping of Ir-PMO.

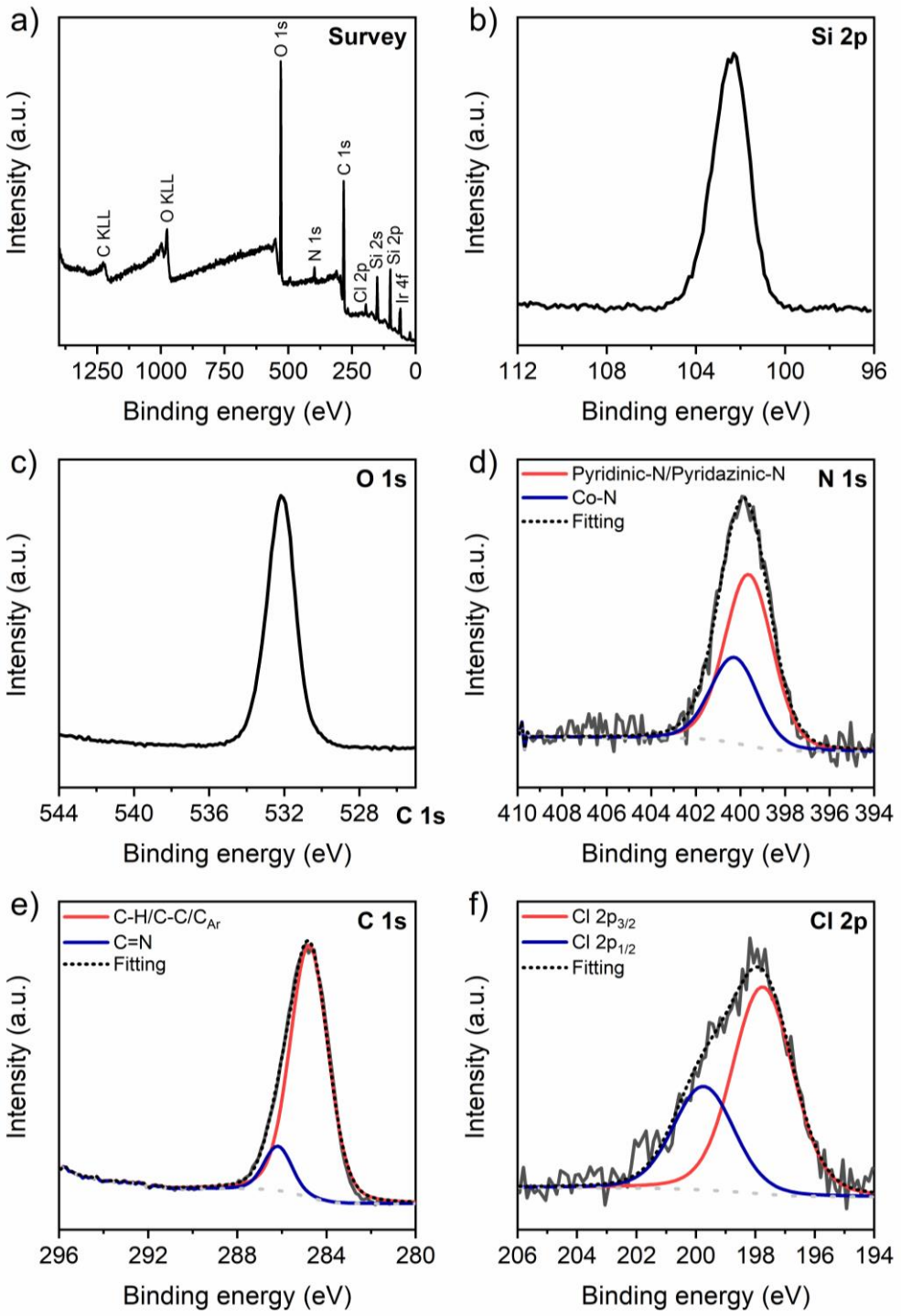

Figure S14. (a) Survey spectra, (b) Si 2p, (c) O 1s and (d) C 1s, (e) N1s and Cl 2p XPS spectra of Ir-PMO.

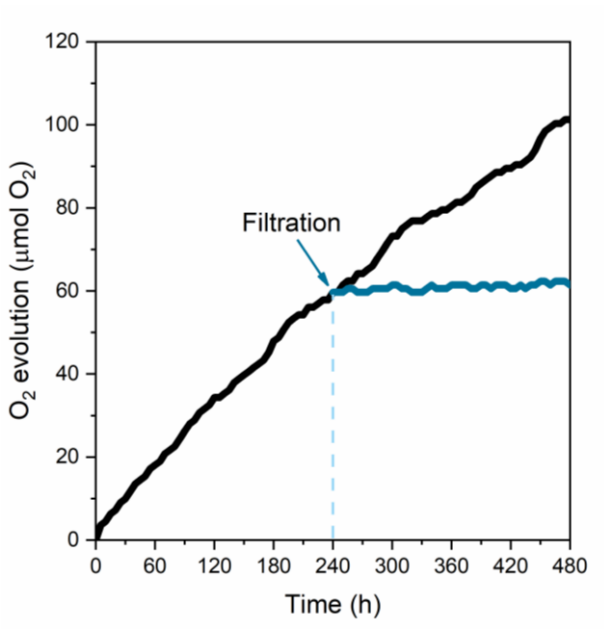

Figure S15. Leaching test for Ir-PMO. The heterogeneous catalyst was filtered after 4h reaction. Black trace shows the normal course of the reaction. Blue trace shows negligible activity of the filtrate during an additional 4h extended period.

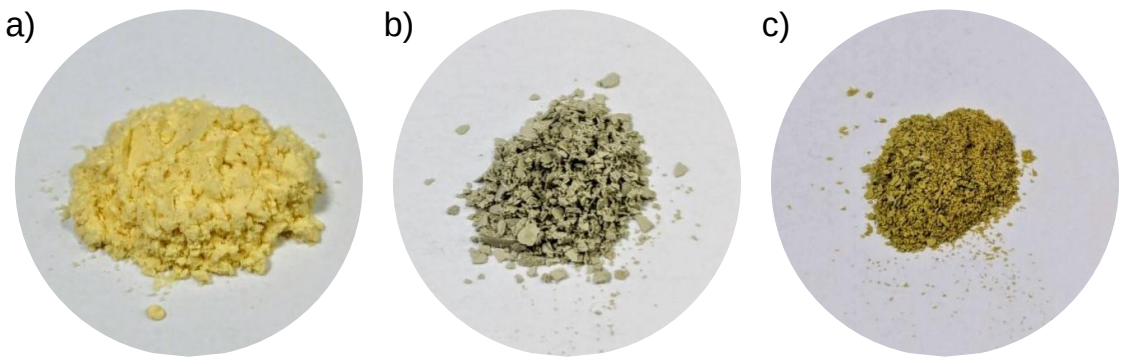

Figure S16. Photograph of: (a) as-synthesized Ir-PMO, (b) post-catalysis Ir-PMO, and (c) post-catalysis Ir-PMO after H_2O/EtOH washing step.

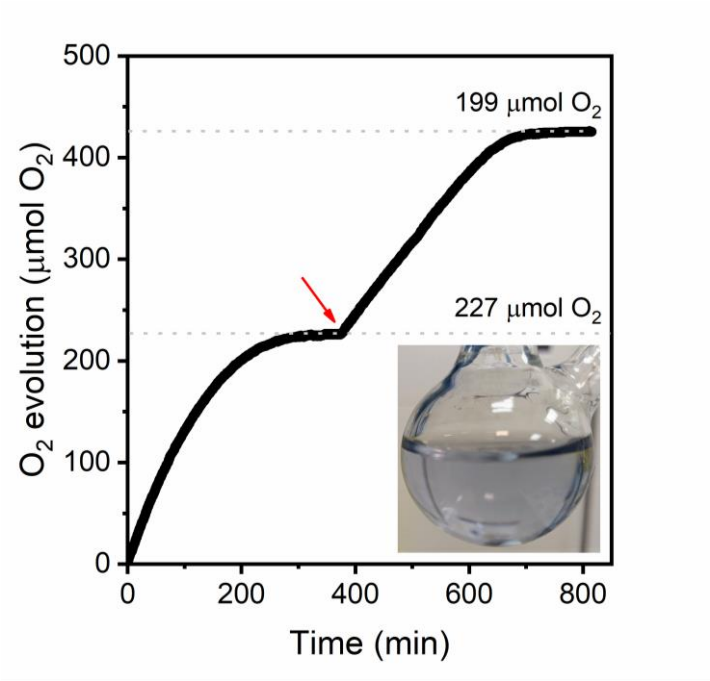

Figure S17. (a) Time course oxygen evolution curve of [IrCp*Cl(dppz)]Cl. Arrows indicate the addition of fresh 100 mM CAN. Inset shows blue coloured solution after cerium-driven WOR. Experimental conditions: 100 mM CAN in HNO_3 (10 mL, 0.1 M, pH = 1) with 72μM [IrCp*Cl(dppz)]Cl (0.72 μmol Ir), [CAN]:[Ir] = 1389.

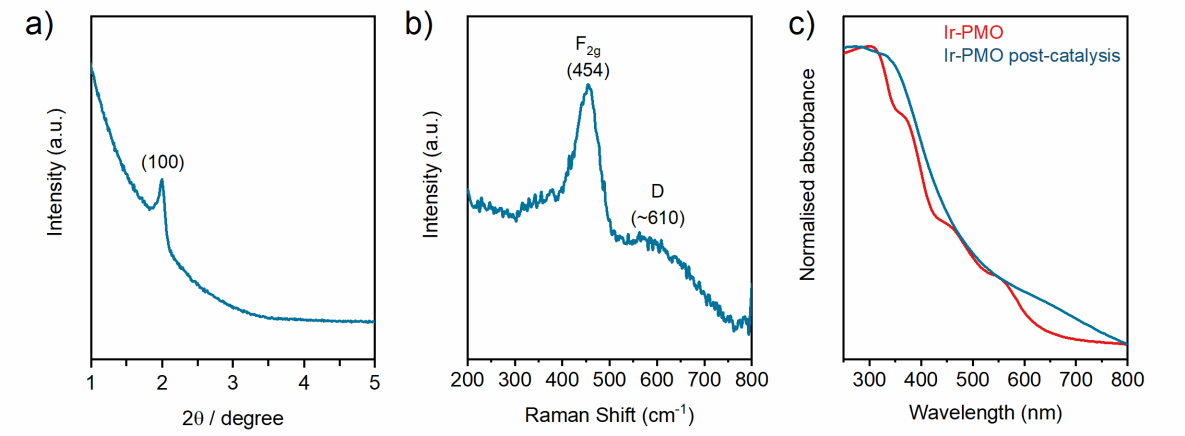

Figure S18. (a) Powder X-ray diffraction pattern, (b) Raman spectrum, and (c) UV–vis diffuse reflectance spectra of Ir-PMO after six catalytic cycles.

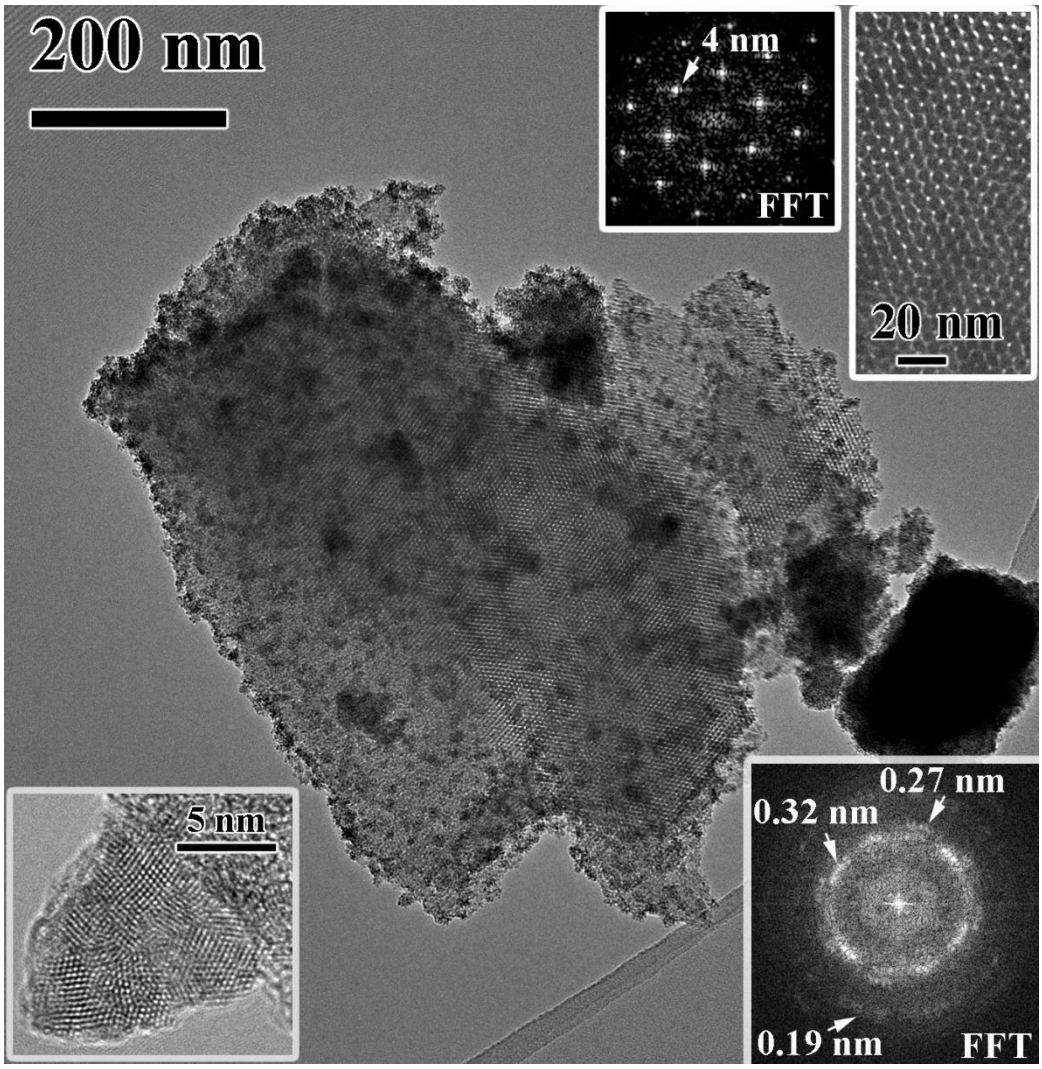

Figure S19. TEM image of Ir-PMO after six catalytic cycles. The insets display magnified views of the retained highly ordered hexagonal mesostructure (along with the corresponding FFT diagram at 20 nm magnification). FFT diagram pattern of an individual nanoparticle (right bottom inset) exhibits a ring whose d spacing are 0.32, 0.27 and 0.19 nm characteristic of (111), (200) and (220) CeO_2 diffraction planes.

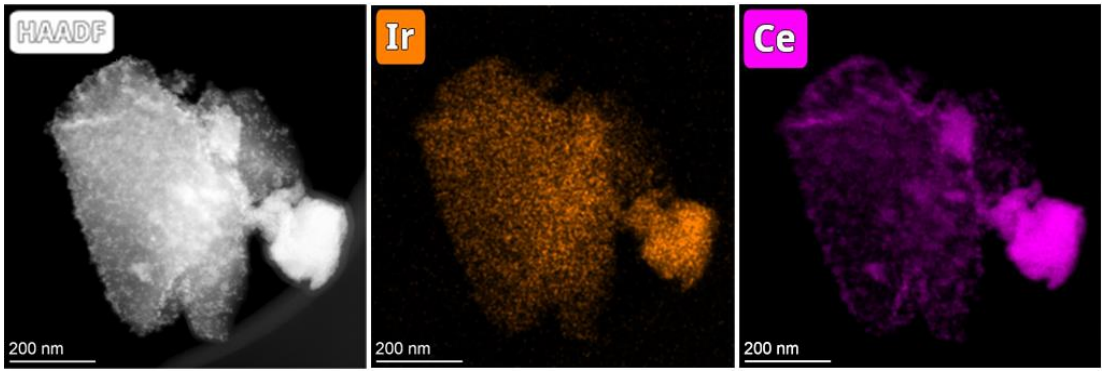

Figure S20. HAADF-STEM image and EDS elemental mapping of Ir-PMO after six catalytic cycles.

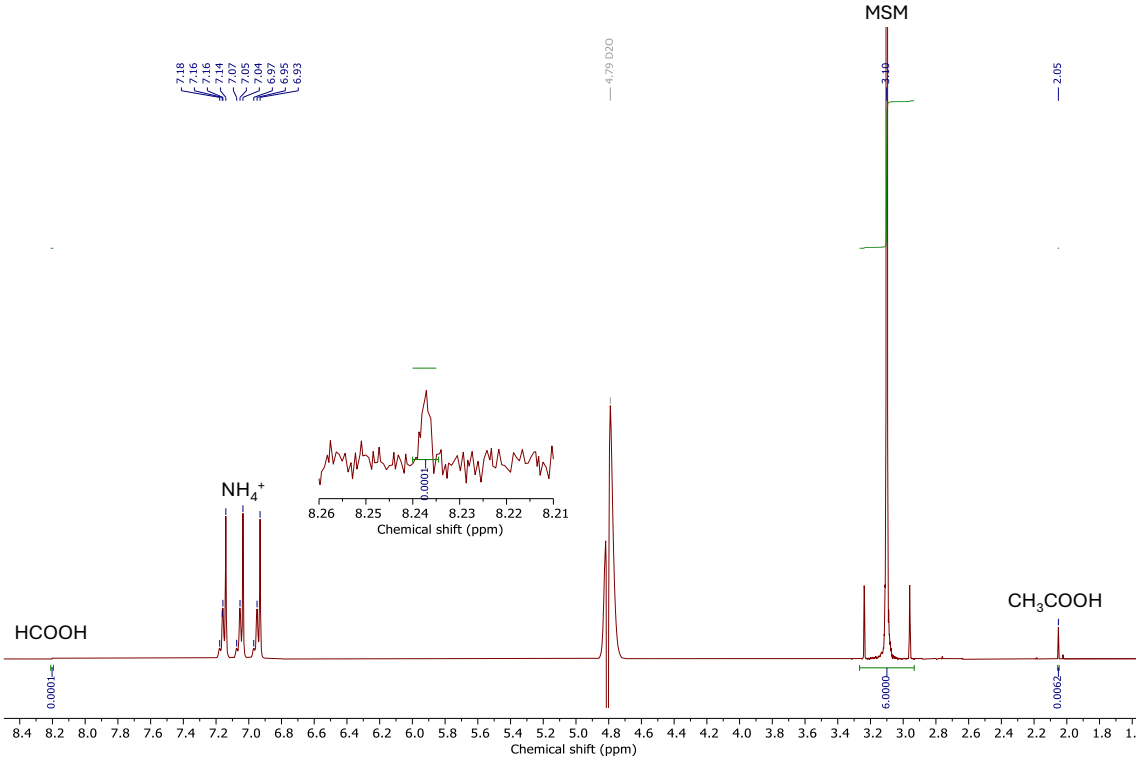

Figure S21. ^{1}H NMR spectrum of the solution resulted from WOR using Ir-PMO after 24 h of a typical catalytic run. Oxidative degradation of Cp* rings were quantified by integration of the acetic and formic acid ^{1}H NMR peaks using methylsulfonylmethane as an internal standard.

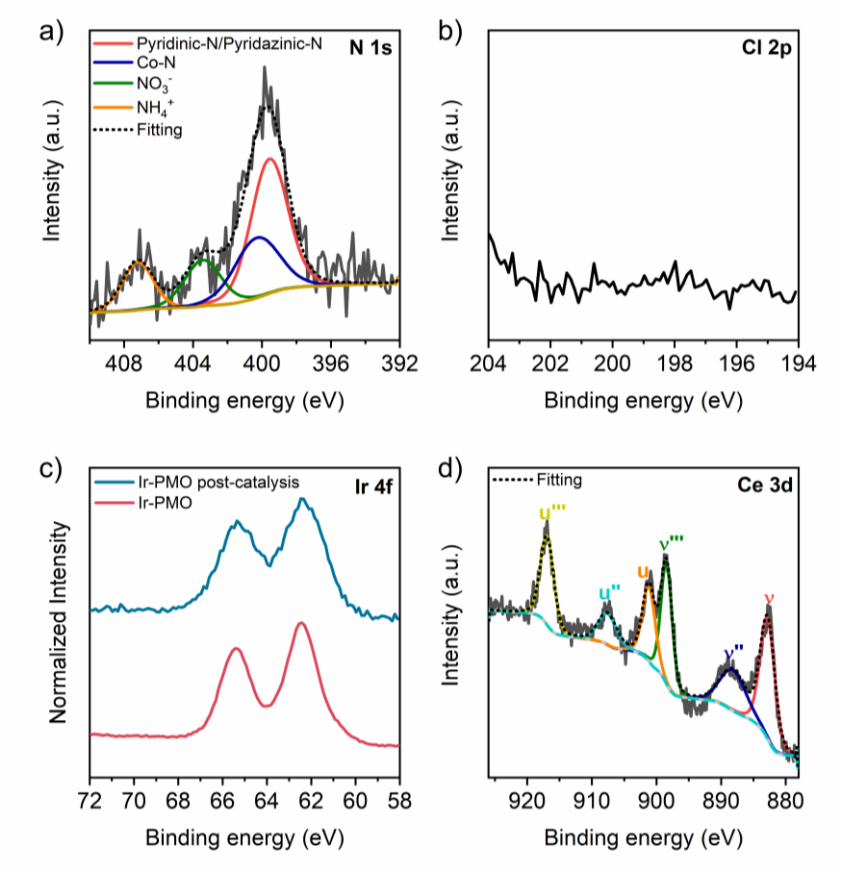

Figure S22. (a) N1s, (b) Cl 2p, (c) Ir 4f and (d) Ce 4f XPS spectra of Ir-PMO after six catalytic cycles.

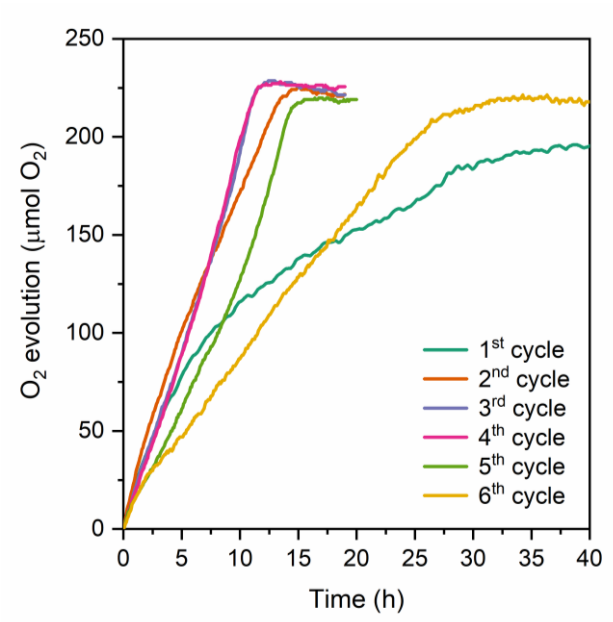

Figure S23. Time dependence oxygen evolution curves for Ir-SBA over six consecutive catalytic cycles. Experimental conditions: 100 mM CAN in HNO_3 (10 mL, 0.1 M, pH = 1) with Ir-PMO (5mg, 0.72 μmol Ir).

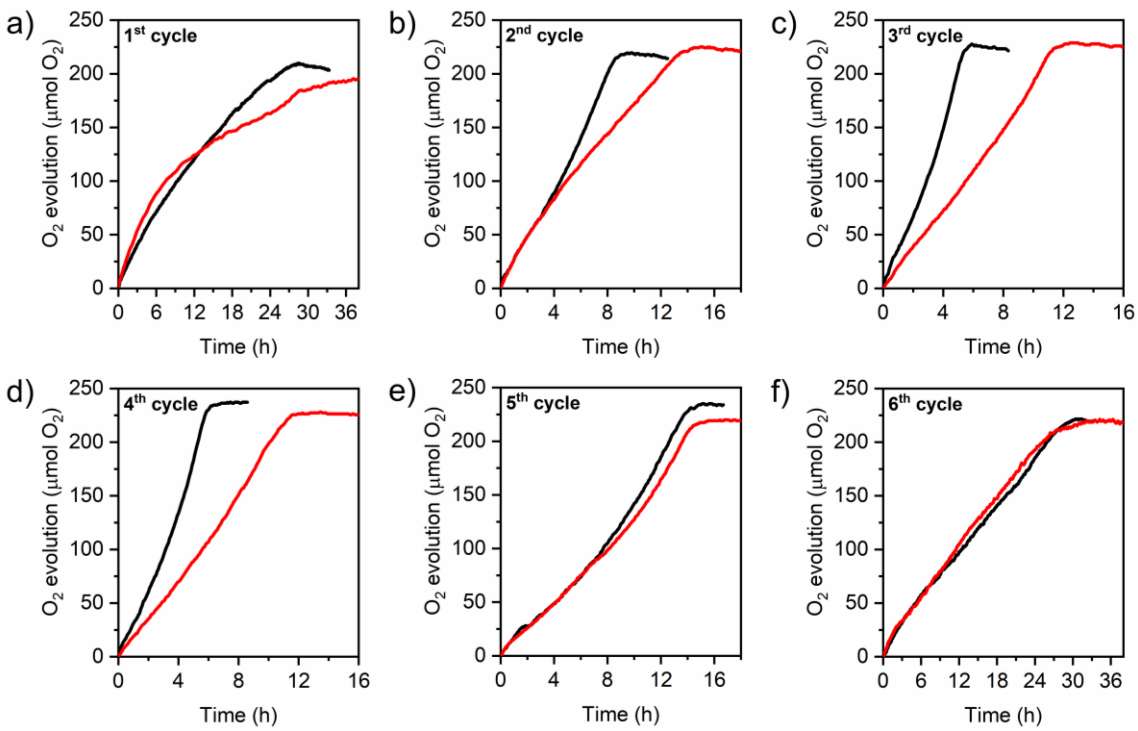

Figure S24. Time dependence oxygen evolution curves for Ir-PMO (black trace) and Ir-SBA (red trace) during six consecutive catalytic cycles. Experimental conditions: 100 mM CAN in HNO_3 (10 mL, 0.1 M, pH = 1) with 0.72 μmol Ir catalyst.

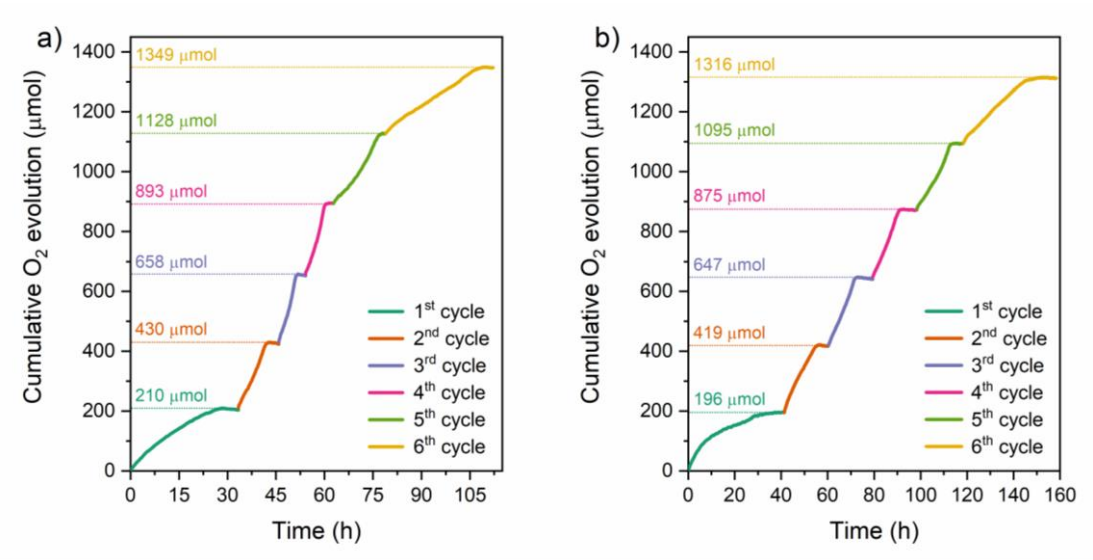

Figure S25. Cumulative time dependence O_2 evolution curves over six consecutive catalytic cycles for (a) Ir-PMO and (b) Ir-SBA.

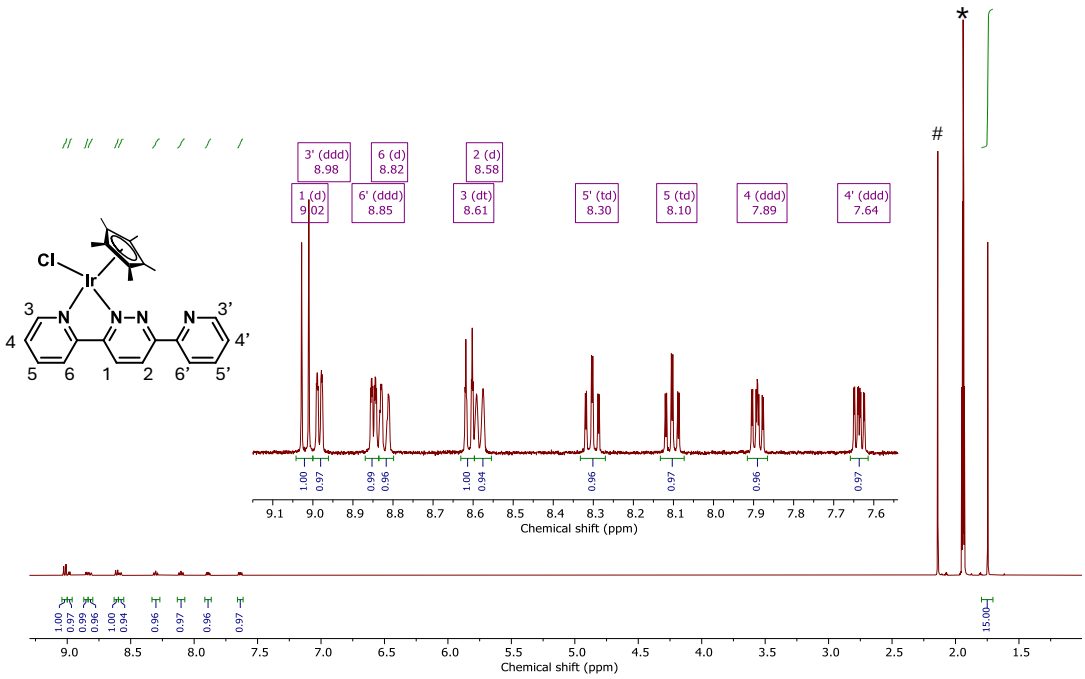

Figure S26. ^{1}H NMR spectrum of [IrCp*Cl(dppz)]Cl in CD_3CN. The symbols, # and * indicate proton peaks of residual H_2O, and residual protons in the acetonitrile-d_3, respectively. Magnification of the downfield region (7.5−9.2 ppm) of the spectrum is shown in the inset.

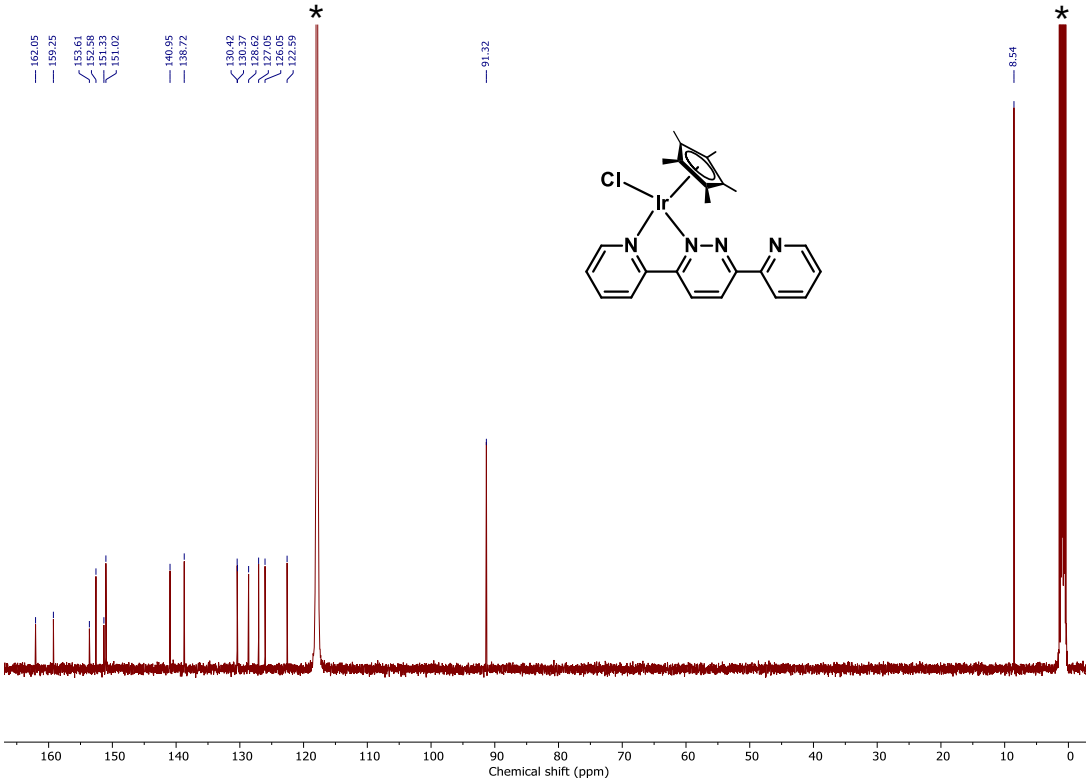

Figure S27. ^{13}C NMR spectrum of [IrCp*Cl(dppz)]Cl in CD_3CN. Residual solvent signals of acetonitrile-d_3 are indicated with asterisks (*).

3. Supporting Tables

Table S1. Crystal data and structure refinement for [IrCp*Cl(dppz)]Cl

Systematic name	[IrCp*Cl(dppz)]Cl
Moiety formula	C_{24} H_{25} Cl Ir N_4, Cl, H_2 O
Sum formula	C_{24} H_{27} Cl_2 Ir N_4 O
Formula weight	650.59
Temperature/K	173.00
Crystal system	orthorhombic
Space group	*Aea*2
a/Å	15.5791(7)
b/Å	37.5967(17)
c/Å	8.1606(4)
α/°	90
β/°	90
γ/°	90
Volume/Å^3	4779.8(4)
Z	8
ρ_{calc}g/cm^3	1.808
μ/mm^{-1}	13.063
F(000)	2544.0
Crystal size/mm^3	0.226 × 0.172 × 0.021
Radiation	CuKα (λ = 1.54178 Å)
2Θ range for data collection/°	7.37 to 144.778
d_{min}	0.81
Index ranges	-19 ≤ h ≤ 19, -46 ≤ k ≤ 46, -9 ≤ l ≤ 10
Reflections collected	25817
Independent reflections	4519 [R_{int} = 0.0315, R_{sigma} = 0.0268]
Absorption correction	Multi-scan
Data/restraints/parameters	4519/1/298
Goodness-of-fit on F^2	1.109
Final R indexes [I>=2σ (I)]	R_1 = 0.0165, wR_2 = 0.0447
Final R indexes [all data]	R_1 = 0.0165, wR_2 = 0.0447
Largest diff. peak/hole / e Å^{-3}	0.82/-0.79
Flack parameter	0.065(11)

Table S2. Bond Lengths for [IrCp*Cl(dppz)]Cl.

Atom	Atom	Length/Å	Atom	Atom	Length/Å
Ir01	Cl1	2.4000(11)	C5	C6	1.465(5)
Ir01	N1	2.097(3)	C6	C7	1.400(5)
Ir01	N2	2.089(3)	C7	C8	1.368(6)
Ir01	C15	2.159(3)	C8	C9	1.403(5)
Ir01	C16	2.166(5)	C9	C10	1.484(5)
Ir01	C17	2.168(4)	C10	C11	1.390(5)
Ir01	C18	2.187(3)	C11	C12	1.384(6)
Ir01	C19	2.171(3)	C12	C13	1.379(7)
N1	C1	1.340(5)	C13	C14	1.385(7)
N1	C5	1.356(4)	C15	C16	1.433(6)
N2	N3	1.335(4)	C15	C19	1.458(5)
N2	C6	1.335(4)	C15	C20	1.493(5)
N3	C9	1.336(5)	C16	C17	1.450(6)
N4	C10	1.335(5)	C16	C21	1.476(6)
N4	C14	1.343(5)	C17	C18	1.437(5)
C1	C2	1.389(6)	C17	C22	1.499(6)
C2	C3	1.388(5)	C18	C19	1.435(5)
C3	C4	1.384(6)	C18	C23	1.489(5)
C4	C5	1.388(5)	C19	C24	1.487(5)

Table S3. Bond Angles for [IrCp*Cl(dppz)]Cl.

Atom	Atom	Atom	Angle/°	Atom	Atom	Atom	Angle/°
N1	Ir01	Cl1	85.57(8)	N2	C6	C7	121.2(3)
N1	Ir01	C15	98.91(12)	C7	C6	C5	123.5(3)
N1	Ir01	C16	124.38(13)	C8	C7	C6	117.1(3)
N1	Ir01	C17	163.00(14)	C7	C8	C9	118.7(4)
N1	Ir01	C18	141.76(13)	N3	C9	C8	122.6(3)
N1	Ir01	C19	106.91(13)	N3	C9	C10	117.4(3)
N2	Ir01	Cl1	87.00(8)	C8	C9	C10	120.0(3)
N2	Ir01	N1	76.72(11)	N4	C10	C9	114.4(3)
N2	Ir01	C15	124.09(12)	N4	C10	C11	123.0(3)
N2	Ir01	C16	98.50(13)	C11	C10	C9	122.6(4)
N2	Ir01	C17	106.50(13)	C12	C11	C10	118.2(4)
N2	Ir01	C18	141.43(13)	C13	C12	C11	119.8(4)
N2	Ir01	C19	162.90(13)	C12	C13	C14	117.9(4)
C15	Ir01	Cl1	148.86(10)	N4	C14	C13	123.5(4)
C15	Ir01	C16	38.70(15)	C16	C15	Ir01	70.9(3)
C15	Ir01	C17	65.19(16)	C16	C15	C19	108.3(3)
C15	Ir01	C18	64.77(13)	C16	C15	C20	125.6(4)
C15	Ir01	C19	39.34(13)	C19	C15	Ir01	70.8(2)
C16	Ir01	Cl1	150.05(11)	C19	C15	C20	126.0(3)
C16	Ir01	C17	39.08(15)	C20	C15	Ir01	125.2(3)
C16	Ir01	C18	64.76(14)	C15	C16	Ir01	70.4(2)
C16	Ir01	C19	65.41(14)	C15	C16	C17	107.9(4)
C17	Ir01	Cl1	111.11(11)	C15	C16	C21	126.9(4)
C17	Ir01	C18	38.54(15)	C17	C16	Ir01	70.5(3)
C17	Ir01	C19	65.18(14)	C17	C16	C21	125.2(4)
C18	Ir01	Cl1	92.77(10)	C21	C16	Ir01	126.0(3)
C19	Ir01	Cl1	109.81(10)	C16	C17	Ir01	70.4(2)
C19	Ir01	C18	38.46(13)	C16	C17	C22	125.3(4)
C1	N1	Ir01	124.5(3)	C18	C17	Ir01	71.4(2)
C1	N1	C5	119.1(3)	C18	C17	C16	107.7(3)
C5	N1	Ir01	116.4(2)	C18	C17	C22	126.8(4)
N3	N2	Ir01	120.3(2)	C22	C17	Ir01	128.0(3)
N3	N2	C6	122.6(3)	C17	C18	Ir01	70.0(2)
C6	N2	Ir01	117.0(2)	C17	C18	C23	127.1(3)
N2	N3	C9	117.8(3)	C19	C18	Ir01	70.20(18)
C10	N4	C14	117.5(4)	C19	C18	C17	108.9(3)
N1	C1	C2	121.8(4)	C19	C18	C23	124.0(3)
C3	C2	C1	119.1(4)	C23	C18	Ir01	125.5(3)
C4	C3	C2	119.3(4)	C15	C19	Ir01	69.9(2)
C3	C4	C5	118.8(4)	C15	C19	C24	127.6(3)
N1	C5	C4	121.9(3)	C18	C19	Ir01	71.34(18)
N1	C5	C6	114.4(3)	C18	C19	C15	107.1(3)
C4	C5	C6	123.7(3)	C18	C19	C24	124.8(3)
N2	C6	C5	115.3(3)	C24	C19	Ir01	129.7(3)

Table S4. Reaction rates for cerium-driven water oxidation of [IrCp*Cl(dppz)]Cl at different [CAN]:[Ir] ratios.[(a)]

[CAN]:[Ir]	TOF (min^{-1})		O_2 evolution (μmol O_2)	O_2 yield (%)
	CAN depletion[(b)]	O_2 evolution[(c)]		
100	2.50	1.20	15	60
400	2.89	1.93	76	76
1000	2.94	2.41	205	82

[(a)] TOF values were calculated during the first 15 minutes after the addition of the oxidizing agent, except for [CAN]:[Ir] = 100, where the TOF values were determined in the first 5 minutes. [(b)] Monitored by in-situ UV–vis spectroscopy. Conditions: [CAN] = 1 mM and [Ir] = 10 μM for [CAN]:[Ir] = 100; [CAN] = 2 mM and [Ir] = 5 μM for [CAN]:[Ir] = 400; [CAN] = 5 mM and [Ir] = 5 μM for [CAN]:[Ir] = 1000. [(c)] Monitored by differential pressure manometry. Conditions: [CAN] = 15 mM, and [Ir] = 150 μM, 37.5 μM and 15 μM for [CAN]:[Ir] = 100, [CAN]:[Ir] = 400 and [CAN]:[Ir] = 1000, respectively.

Table S5. Comparison of the cerium-driven water oxidation catalytic activity for reported half-sandwiched Ir(III) WOCs.[(a)]

Entry	Catalyst	TOF (min^{-1})	O_2 yield (%)	Reference
1	[IrCp*(bpy)Cl]Cl	4	83	[4]
2	[IrCp*(dpa)Cl]Cl	25	94	[4]
3	[IrCp*(pic)NO_3]	10	70	[5]
4	[IrCp*(pic-*3*OH)NO_3][(b)]	23	90	[5]
5	[IrCp*(pic-*4*OH)NO_3][(b)]	25	65	[5]
6	[IrCp*(pic-*5*OH)NO_3][(b)]	24	100	[5]
7	[IrCp*(pic-*6*OH)NO_3][(b)]	22	75	[5]
8	[IrCp*Cl(dppz)]Cl	2.4	82	*This work*

Abbreviations: bpy = 2,2'-bipyridine; dpa = *2,2'-dipyridylamine*; pic = picolinate = κ^2-pyridine-2-carboxylic acid; dppz = 3,6-dipyridin-2-ylpyridazine. [(a)] [CAN]:[Ir] = 1000. [(b)] In (pic-*x*OH), *x* represents the position at which the -OH group is substituted on the pyridine ring.

Table S6. Iridium loading values of Ir-PMO catalyst estimated by ICP-MS analysis.

Sample	Ir/dppz molar ratio	Ir loading (mmol g^{-1})	Coordinated dppz units[(a)] (%)
Ir-PMO	1	0.240	59.7
	1.5	0.258	64.2
	2	0.260	64.6

[(a)]dppz content: 0.402 mmol g^{-1}

Table S7. Textural properties of NdppzPMO and Ir-PMO.

Sample	S_{BET} (m^2 g^{-1})	V_P (cm^3 g^{-1})	D_P (nm)
NdppzPMO	865	0.51	2.8
Ir-PMO	612	0.40	2.7

Table S8. Water oxidation catalytic activity for Ir-SBA during six consecutive catalytic cycles.

Reaction Cycle	O_2 evolution (μmol O_2)	O_2 Yield[(a)] (%)	TON	TOF[(b)] (min^{-1})
1st	196	78	272	0.72
2nd	223	89	310	0.72
3rd	228	91	316	0.5
4th	228	91	316	0.48
5th	220	88	305	0.48
6th	221	89	308	0.33

[(a)] Calculated in relation with the theorical maximum amount of 250 μmol oxygen evolved. [(b)] Calculated in the first 15 min after the addition of oxidising agent. Experimental conditions: 100 mM CAN in HNO_3 (10 mL, 0.1 M, pH = 1) using Ir-SBA (5 mg, 0.72 μmol Ir)

4. References

1 O. V. Dolomanov, L. J. Bourhis, R. J. Gildea, J. A. K. Howard and H. Puschmann, *J. Appl. Crystallogr.*, 2009, **42**, 339–341.

2 G. M. Sheldrick, *Acta Crystallogr. Sect. A Found. Adv.*, 2015, **71**, 3–8.

3 G. M. Sheldrick, *Acta Crystallogr. Sect. C Struct. Chem.*, 2015, **71**, 3–8.

4 A. Bucci, G. Menendez Rodriguez, G. Bellachioma, C. Zuccaccia, A. Poater, L. Cavallo and A. Macchioni, *ACS Catal.*, 2016, **6**, 4559–4563.

5 G. Menendez Rodriguez, A. Bucci, R. Hutchinson, G. Bellachioma, C. Zuccaccia, S. Giovagnoli, H. Idriss and A. Macchioni, *ACS Energy Lett.*, 2017, **2**, 105–110.